# Analytical Analysis of a Radial Flux Air-Cored Permanent Magnet Machine with a Double-Sided Rotor and Non-overlapping Double-layer Windings

P. J. Randewijk, M. J. Kamper

***Abstract*—The radial flux density in the stator region of the Radial Flux Air-cored Permanent Magnet (RFAPM) machine can be calculated analytically using the subdomain analysis method. From the analytical solution the optimum pole width of the permanent magnets, that would produce a quasi sinusoidal radial flux density distribution in the stator region, can easily be calculated. The requirement for a sinusoidal radial flux density distribution in the stator region, is that it allows for a voltage – and torque constant to be defined for the RFAPM machine. This not only simplifies the design procedure in terms of sizing the RFAPM machine, but also simplifies the control aspects of the RFAPM machine. Furthermore, the torque developed by a RFAPM machine, specifically with regard to the size and shape of the ripple torque is also calculated analytically using the Lorentz method. All the analytical results are benchmarked against Finite Element Modelling (FEM).**

***Index Terms*—air-cored, electrical machine constants, non-overlapping windings, permanent magnets, radial flux density distribution, ripple torque**

## NOMENCLATURE

### A. Roman Symbols

| | |
|---|---|
| $a$ | number of parallel circuits per phase |
| $A$ | magnetic vector potential, (Wb/m) |
| $B_g$ | flux density in the airgap, (T) |
| $B_{rem}$ | remanent flux density of the permanent magnets, (T) |
| $E_f$ | back-EMF voltage, (V) |
| $h$ | height/thickness of the stator coils, (m) |
| $h_m$ | magnet height/thickness, (m) |
| $h_y$ | yoke height/thickness, (m) |
| $H_c$ | coercivity of a permanent magnet, (At/m) |
| $H_g$ | magnetic field intensity in the airgap, (At/m) |
| $H_m$ | magnetic field intensity in the permanent magnet, (At/m) |
| $I_s$ | stator current space vector, (A) |
| $k_\Delta$ | coil side-width factor |
| $k_m$ | the magnet- (or pole) arc-to-pole-pitch-ratio |
| $k_E$ | voltage constant, (V/rad/s) |
| $k_T$ | torque constant, (Nm/A) |
| $k_w$ | general winding factor |
| $k_{w,pitch}$ | winding pitch factor |
| $k_{w,slot}$ | winding slot width factor |
| $\ell$ | active copper length of the stator conductors, (m) |
| $\ell_c$ | mean magnetic flux path length in the iron core, (m) |
| $\ell_g$ | airgap length, (m) |
| $M_0$ | residual magnetisation, (A/m) |
| $n$ | conductor density distribution |
| $N$ | number of turns per coil |
| $p$ | number of pole pairs |
| $q$ | number of coils per phase |
| $Q$ | total number of coils ($Q = 3q$) |
| $r_{cm}$ | the radius as measured to the centre of the magnets, (m) |
| $r_n$ | nominal stator radius, (m) |

### B. Greek Symbols

| | |
|---|---|
| $\Delta$ | $\frac{1}{2}$ coil side-width angle of the stator coils, (rad) |
| $\lambda_1$ | flux-linkage of a single turn, (Wb-turns) |
| $\Lambda$ | total flux-linkage per phase, (Wb-turns) |
| $\mu_{recoil}$ | recoil permeability ($\mu_0\mu_{r_{recoil}}$) |
| $\mu_{r_{recoil}}$ | relative recoil permeability |
| $\phi$ | azimuthal axis in cylindrical coordinates |
| $\tau_q$ | coil pitch angle, (rad) |
| $\tau_{q,res}$ | resultant coil pitch angle, (rad) |
| $\theta_m$ | pole/magnet width angle, (rad) |
| $\theta_p$ | pole/magnet width angle, (rad) |

### C. Accents or attributes

| | |
|---|---|
| $\vec{\mathbf{A}}$ | a vector field |
| $\hat{A}$ | amplitude or peak value |

### D. Subscripts

| | |
|---|---|
| $r\|\phi\|z$ | the cylindrical coordinates components |

## I. INTRODUCTION

THE Radial Flux Air-Cored Permanent Magnet (RFAPM) machine with a double-sided rotor and non-overlapping windings is shown in Fig. 1 and was first presented in [1]. The RFAPM machine was conceived with medium to small direct drive wind generators in mind and is basically a dual of the Axial Flux Air-Cored Permanent Magnet (AFAPM) machine that also utilises a double-sided rotor and non-overlapping windings [2].

These RFAPM and AFAPM machines are designed with efficiency in mind. Due to the air-cored stator windings there are no stator iron losses in these machines. In addition, by

P. J. Randewijk is with the Department of Electrical and Electronic Engineering, Stellenbosch University, Stellenbosch, South Africa (e-mail: pjrandewijk@ieee.org)

M. J. Kamper is with the Department of Electrical and Electronic Engineering, Stellenbosch University, Stellenbosch, South Africa (e-mail: kamper@ieee.org)

978-1-4673-0142-8/12/$26.00 ©2012 IEEE

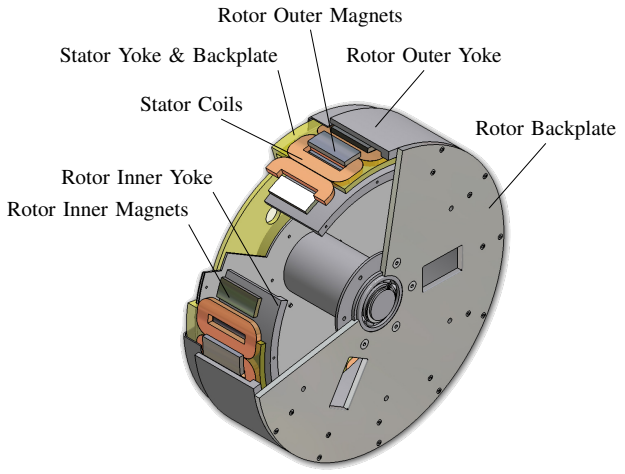


Fig. 1. A 3D view of a 16 pole RFAPM machine with double-layer, non-overlapping, concentrated winding configuration, [5].

using non-overlapping windings, the end-turn winding length and hence the associated copper losses are also minimised, [3]. The air-cored stator also implies no cogging torque, resulting in not only "smooth running", [4], but also very low cut-in wind speeds for wind generator applications. However, the structural integrity of the RFAPM machine's cylindrically shaped rotor yokes [5], is much higher than that of the AFAPM machine's disc shaped rotor yokes [6], resulting in a 36% weight reduction being able to achieve[1] for the RFAPM machine when compared to an AFAPM machine for the same 7 kW rating, [5].

The design procedure for the RFAPM machine that was presented by [5] was reliant on Finite Element Modelling (FEM) in order to calculate the radial flux density distribution. In this paper the radial flux density distribution of the RFAPM machine is solved analytically using the subdomain analysis method, [7], which is more than two orders of magnitude faster than using FEM. The analytical solution to the magnetic fields allows us to calculate the optimum permanent magnet (PM) pole width that would result in a quasi sinusoidal radial flux density distribution in the stator region of the machine very efficiently.

It will be shown that with a sinusoidal radial flux density distribution, a voltage constant can deduced from which the steady state back-EMF of the RFAPM machine can easily be calculated from the mechanical steady state speed of the machine. This also results in a torque constant (equal to the voltage constant) from which the steady state mechanical torque can be calculated from the stator current space vector. From a design perspective, these constants, expressed in terms of some of the key machine parameters, allows for the quick sizing of the RFAPM machine for a given application. Furthermore, from a control perspective, these constants allow for simple control, similar to a normal brushless DC machine, to be performed on the RFAPM machine.

A torque equation for the torque developed by the RFAPM machine using the Lorentz method that includes the ripple torque component is also derived in this paper. No evidence in the literature could be found for this ever being done for a RFAPM machine.

The Lorentz method is much more computationally efficient, than the Maxwell stress tensor (MST) method [8], in that it only requires the radial flux density component caused by the PMs to be solved for the torque calculation. The Lorentz method could also be applied to AFAPM machines (or any air-cored machine for that matter), in which case its computational efficiency, compared to the MST method used in [9] or FEM used in [10] for reduced torque ripple optimisation, would be quite evident.

It must be emphasised that the Lorentz method can only be using for air-cored machines. In iron-cored machines, due to the additional cogging torque, other calculation methods should be used, [8] and [11].

[1]The total mass of the RFAPM machine was 59 kg compared to the 92 kg of an equivalent AFAPM machine.

## II. Analytical Field Analysis

The different subdomains or regions of the RFAPM machine are shown in Fig. 2, which depicts a linear 2D representation of the RFAPM machine as shown in Fig. 1. The governing equations for the different subdomains of the RFAPM machine, are given in Tabel I.

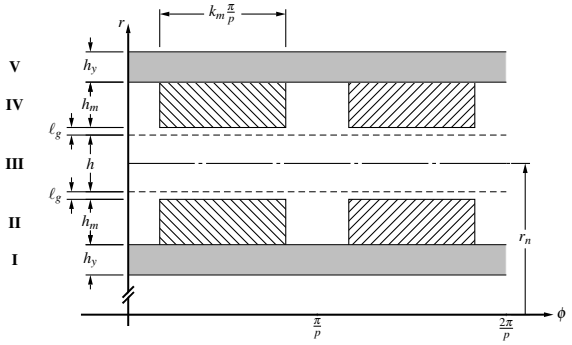


Fig. 2. A linear representation of the different subdomains or regions.

| Subdomain | Description | $\mu_r$ | Governing equation |
|---|---|---|---|
| **I** | Rotor Yoke | $\mu_y$ | $\nabla^2\vec{\mathbf{A}} = 0$ |
| **II** | Magnets | 1 | $\nabla^2\vec{\mathbf{A}} = -\mu_0\left(\nabla\times\vec{\mathbf{M}}_0\right)$ |
| **III** | Stator | 1 | $\nabla^2\vec{\mathbf{A}} = 0$ |
| **IV** | Magnets | 1 | $\nabla^2\vec{\mathbf{A}} = -\mu_0\left(\nabla\times\vec{\mathbf{M}}_0\right)$ |
| **V** | Rotor Yoke | $\mu_y$ | $\nabla^2\vec{\mathbf{A}} = 0$ |

TABLE I
THE GOVERNING EQUATIONS FOR THE DIFFERENT SUBDOMAINS.

In Tabel II, the key dimension of the RFAPM machine are shown with respect to the 2D linear representation of the machine as shown in Fig. 2. The analytical analysis presented in this paper together with the FEM verification will be done using these values.

| Description | Symbol | Value |
|---|---|---|
| Number of pole-pairs | p | 16 |
| Number of coils per phase | q | 8 |
| Nominal stator radius | $r_n$ | 232 mm |
| Active stator/copper length | $\ell$ | 76 mm |
| Stator coil thickness/height | $h$ | 10 mm |
| N48 NdFeB PM thickness/height | $h_m$ | 8.2 mm |
| Rotor yoke thickness/height | $h_y$ | 10 mm |
| Air-gap length | $\ell_g$ | 10 mm |

TABLE II
KEY DIMENSION FOR THE RFAPM MACHINE UNDER CONSIDERATION.

For the analytical analysis, the following assumptions were made. Firstly, for the NdFeB grade N48 PMs used, the recoil permeability was taken as "unity", whilst the permeability of the rotor yoke's back iron was regarded to be constant, [12]. The latter, although ignoring saturation, allows us to solve the flux density in the rotor yoke to estimate the amount of saturation in the yokes so as to gauge the accuracy of the solution. Finally, to simplify the mathematics in the analytical solution of the magnetic vector potential the residual magnetisation was also approximated to

$$\vec{\mathbf{M}}_0 \approx \frac{r_{cm}}{r} \cdot \frac{\vec{\mathbf{B}}_{rem}}{\mu_0} \tag{1}$$

with $r_{cm}$ the radius measured to the centre of each magnet and $\vec{\mathbf{B}}_{rem}$ the remanent flux density of the PMs used, [13].

For the annulus shaped subdomain structures, the general 2-D solution of the magnetic vector potential in all the regions has only a $z$-axis solution and is of the following from

$$A_{z,gen}(r,\phi) = \sum_{m=1,3,5,\ldots}^{\infty} \left(C_m r^{mp} + D_m r^{-mp}\right) \cos mp\phi \quad , \tag{2}$$

with the particular solution in regions II and IV, given by

$$A_{z,part}(r,\phi) = \sum_{m=1,3,5,\ldots}^{\infty} G_m \cos mp\phi \quad , \tag{3}$$

with

$$G_m = -\frac{4 r_{cm} B_{rem} \cos mp\beta}{m^2 p \pi} \tag{4}$$

and

$$\beta = \left(\frac{1-k_m}{2}\right)\frac{\pi}{p} \quad , \tag{5}$$

with $k_m$ the magnet- (or pole) arc-to-pole-pitch-ratio as graphically shown in Fig. 2.

The relationship between the magnetic vector potential, the flux density and the magnetic field intensity, is given by

$$\vec{\mathbf{B}} = \boldsymbol{\nabla} \times \vec{\mathbf{A}} \quad \text{and} \tag{6}$$

$$\vec{\mathbf{H}} = \frac{\vec{\mathbf{B}}}{\mu} \ . \tag{7}$$

Using the following boundary conditions,

$$A_z^{(v)} = 0 \quad , \tag{8}$$

$$B_r^{(v)} = B_r^{(v+1)} \quad \text{and} \tag{9}$$

$$H_\phi^{(v)} = H_\phi^{(v+1)} \quad , \tag{10}$$

with (8) applied to the inner and outer boundary and (9) and (10) to the remaining boundaries situated between two subdomains, the boundary matrix will have the following form (only shown for the first five coefficients):

$$\begin{bmatrix} r_i^{mp} & r_i^{-mp} & & \cdots \\ r_{ii}^{mp} & r_{ii}^{-mp} & -r_{ii}^{mp} & \cdots \\ r_{ii}^{mp-1} & -r_{ii}^{-mp-1} & -r_{ii}^{mp-1} & \cdots \\ & & r_{iii}^{mp} & \cdots \\ & & r_{iii}^{mp-1} & \cdots \\ \vdots & \vdots & \vdots & \ddots \end{bmatrix} \cdot \begin{bmatrix} C_m^I \\ D_m^I \\ C_m^{II} \\ D_m^{II} \\ C_m^{III} \\ \vdots \end{bmatrix} = \begin{bmatrix} 0 \\ G_m^{II} \\ 0 \\ -G_m^{II} \\ 0 \\ \vdots \end{bmatrix} \tag{11}$$

The radii at the different boundaries, $r_i$ to $r_{vi}$, can be calculated by the following equations:

$$r_i = r_n - \tfrac{h}{2} - \ell_g - h_m - h_y \tag{12}$$

$$r_{ii} = r_n - \tfrac{h}{2} - \ell_g - h_m \tag{13}$$

$$r_{iii} = r_n - \tfrac{h}{2} - \ell_g \tag{14}$$

$$r_{iv} = r_n + \tfrac{h}{2} + \ell_g \tag{15}$$

$$r_v = r_n + \tfrac{h}{2} + \ell_g + h_m \tag{16}$$

$$r_{vi} = r_n + \tfrac{h}{2} + \ell_g + h_m + h_y \tag{17}$$

From (2) and applying (6), the solution of the radial flux density distribution in the stator region is given by the following

$$B_r(r,\phi) = -\frac{1}{r} \cdot \sum_{m=1,3,5,\ldots}^{\infty} mp(C_m^{III} r^{mp} + D_m^{III} r^{-mp}) \sin mp\phi \quad , \tag{18}$$

with $C_m^{III}$ and $D_m^{III}$ the coefficients in region III (the stator region) obtained from the boundary condition matrix (11).

The space harmonics present in the radial airgap flux density distribution in the centre of the stator winding region can be obtained directly from (18) without the need to perform a FFT, by setting $r{=}r_n$ and substituting $h$ for $m$, so that we can write,

$$\hat{B}_{r,h} = -\frac{hp}{r_n}(C_h^{III} r_n^{hp} + D_h^{III} r_n^{-hp}) \ . \tag{19}$$

The total harmonic distortion (THD) of the radial flux density in the airgap can be calculated as follows:

$$\%\text{THD}_{B_r} = \frac{\sqrt{\sum_{h=2}^{\infty} \hat{B}_{r,h}^2}}{\hat{B}_{r,1}} \times 100\% \tag{20}$$

In [14] the shape of the PMs were optimised by varying the thickness of PM in order to obtain a sinusoidal flux density distribution. It was found that by varying only the PM's pole-arc-width, i.e. effectively $k_m$, the shape of the radial flux density distribution in the centre of the stator could also be made quasi sinusoidal, as is shown in Fig. 3. Although $k_m{=}0.6875$ resulted in the lowest percentage total harmonic distortion (%THD) value for the radial flux density distribution, a final value of $k_m{=}0.7$ was chosen in order to achieve a slightly higher fundamental radial flux density distribution value.

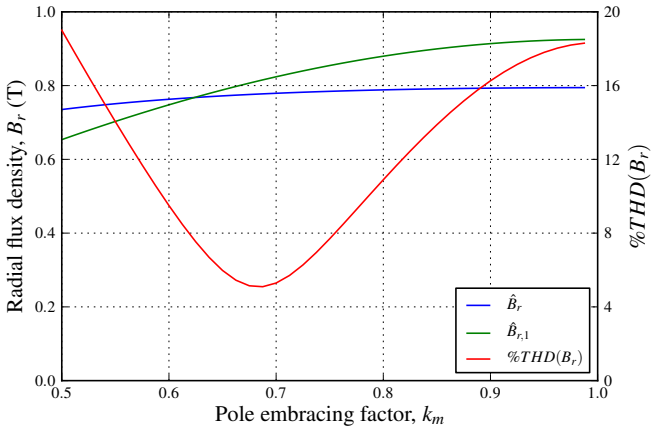


Fig. 3. The magnitude of the peak – and fundamental radial flux density distribution as a function of $k_m$.

From the 2-D analytical analysis with a $k_m$ value of 0.7, the peak value of the radial flux density distribution in

the centre of the stator winding region, $\hat{B}_r$, was calculated as $0.779\,\mathrm{T}$ with the fundamental component, $\hat{B}_{r,1}$ equal to $0.824\,\mathrm{T}$. However, the question arises, "Can we obtain the same result using simple (1-D) equivalent magnetic circuit model?" From Fig. 2, using an equivalent C-type magnetic circuit model, [15] and assuming that fringing can be ignored, thus assuming that the flux density in the PMs, $B_m$, is the approximately same as that in the airgap, $B_g$, that the permeability of the iron yoke is infinity and that average flux path will be in the centre of the PMs, the radial flux density in the airgap can be approximated by the following equation:

$$B_g = \frac{B_{rem}}{\left(1 + \mu_{r_{recoil}} \cdot \frac{2\ell_g + h}{2h_m}\right)} \ , \tag{21}$$

From (21), the flux density inside the airgap, $B_g$, was calculated as $0.788\,\mathrm{T}$ which correlates very closely with the 2-D analysis results. Furthermore, from (21) the PMs' thickness or width, $h_m$, can easily be calculated as follows:

$$h_m = \frac{(\ell_g + \frac{h}{2})\mu_{r_{recoil}}}{\left(\frac{B_{rem}}{B_g} - 1\right)} \ . \tag{22}$$

From the simple (1-D) equivalent magnetic circuit analysis it is however impossible to predict the exact shape of the flux density distribution and hence to calculate the fundamental component of the flux density distribution. This is due to the fact that the 1-D approach of the equivalent magnetic circuit analysis does not take any cognisance of the magnetic pole width or inter pole flux leakage. The calculated flux density values will therefore be exactly the same, whether the magnetic poles span the entire pole pitch or only half the pole pitch.

In Fig. 4 the 2-D analytically calculated radial flux density distribution in the centre and on the edges of the stator region is compared with a Maxwell® 2D FEM solution. The analytically calculated radial flux density values were found to be only 3% higher than those of the FEM solution. This could be attributed to the saturation of the relatively thin rotor yokes used by the RFAPM machine. The analytically calculated flux density values in the rotor yokes reached a maximum of $\approx 2.7\,\mathrm{T}$ at the edges of the PMs compared to just under $2\,\mathrm{T}$ using FEM, a clear indication of saturation occurring in the rotor yokes.

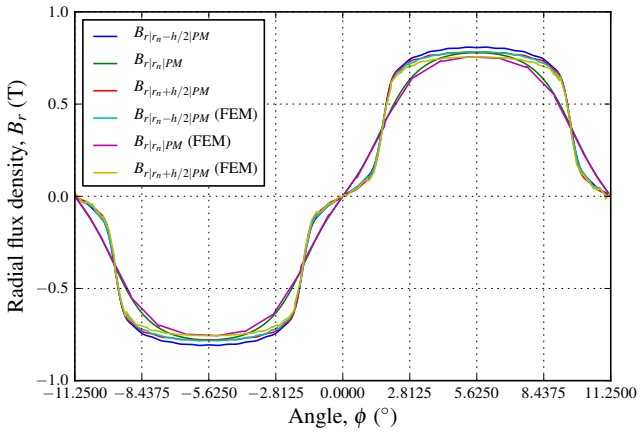


Fig. 4. The analytically calculated radial flux density distribution in the stator region of the RFAPM machine.

## III. Winding Configuration

In Fig. 5 the three-phase winding configuration for a dual-rotor RFAPM machine with non-overlapping double layer windings is shown. The Fourier expansion of the conductor density distribution for phase $a$ can be written as

$$n_a(\phi) = \sum_{n=1}^{\infty} b_n \sin(nq\phi) \tag{23}$$

with

$$b_n = -\frac{2qN}{\pi} \cdot k_{w,n} \tag{24}$$

with the winding factor expanding to

$$k_{w,n} = k_{w,pitch,n} \cdot k_{w,slot,n} \ , \tag{25}$$

with the pitch factor,

$$k_{w,pitch,n} = \sin\left(n(\tfrac{\pi}{3} - \Delta)\right) \tag{26}$$

and the "virtual" slot – or coil side-width factor,

$$k_{w,slot,n} = \frac{\sin(n\Delta)}{n\Delta} \ , \tag{27}$$

with $\Delta$, half the coil side-width angle, as defined in Fig. 5.

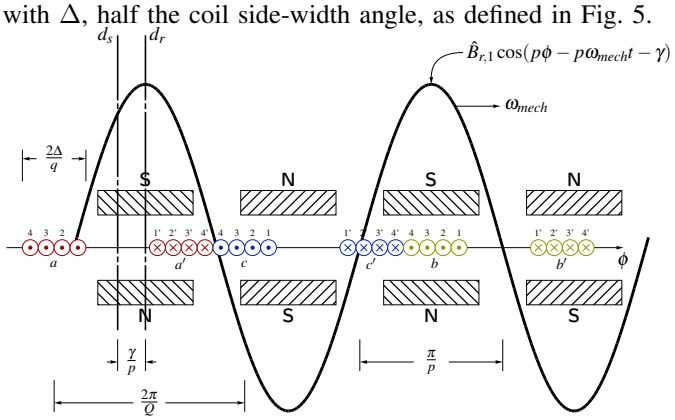


Fig. 5. Three-phase winding configuration for a Dual-Rotor RFAPM machine with non-overlapping double layer windings.

With the number of pole pairs, $p$, equal to twice the number of coils per phase, $q$, due to the non-overlapping winding configuration, the only winding factor harmonics that need to be considered are the second order harmonics, i.e. those with $n{=}2m$.

## IV. Flux-Linkage and Back-EMF Calculation

The flux-linkage for a single turn can be calculated form the magnetic vector potential as follows, [13],

$$\hat{\lambda}_1(r,\phi) = \int_S \boldsymbol{\nabla} \times \vec{\mathbf{A}} \cdot d\vec{\mathbf{s}} \ . \tag{28}$$

From the winding density distribution, (23), and assuming perfectly symmetrical phase windings, the peak value of the flux-linkage for all three phases can be calculated as follows,

$$\hat{\Lambda}_{a,b,c} = \frac{q}{a} \int_{-\frac{1}{2}\tau_{q,res}}^{\frac{1}{2}\tau_{q,res}} n_a(\phi)\hat{\lambda}_1(r,\phi)d\phi \ . \tag{29}$$

If we assume that the magnetic vector potential in the winding region is everywhere the same as in the centre, i.e.

at $r{=}r_n$, the flux-linkage can thus be calculated, from the 2-D analytical field solution, as

$$\hat{\Lambda}_{a,b,c} = \frac{2q\ell}{a}\int_{-\frac{1}{2}\tau_{q,res}}^{\frac{1}{2}\tau_{q,res}} n_a(\phi)A_z(r_n,\phi)d\phi \tag{30}$$

$$= -\frac{2q\ell r_n N}{a}\sum_{m=1}^{\infty} k_{w,2m} b^{III}_{m|A_z} \tag{31}$$

with, from (2),

$$b^{III}_{m|A_z} = C^{III}_m r^{mp} + D^{III}_m r^{-mp}\ . \tag{32}$$

However, if we only consider the fundamental component of the solution, i.e. $m{=}1$, the solution to the flux-linkage can be approximated by

$$\hat{\Lambda}_{a,b,c} \approx \frac{2qr_n\ell N}{ap} k_{w,2}\hat{B}_{r,1}\ . \tag{33}$$

Further, assuming that the machine is rotating at a constant speed of $\omega_{mech}$ and using the approximation for the peak flux-linkage of (33), the back-EMF for each phase can be approximated as

$$e_a = \hat{E}_{a,b,c}\sin\big(p\omega_{mech}t\big) \tag{34}$$

$$e_b = \hat{E}_{a,b,c}\sin\big(p\omega_{mech}t - \tfrac{2\pi}{3}\big) \tag{35}$$

$$e_b = \hat{E}_{a,b,c}\sin\big(p\omega_{mech}t - \tfrac{4\pi}{3}\big) \tag{36}$$

with

$$\hat{E}_{a,b,c} \approx -\frac{2q\omega_{mech}r_n\ell N}{a} k_{w,2}\hat{B}_{r,1}\ . \tag{37}$$

The general solution to the back-EMF, can thus be written as

$$\hat{E}_f = k_E\omega_{mech} \tag{38}$$

with the back-EMF

$$\hat{E}_f = \hat{E}_{a,b,c} \tag{39}$$

and the voltage constants,

$$k_E = \frac{2qr_n\ell N}{a} k_{w,2}\hat{B}_{r,1}\ . \tag{40}$$

In Fig. 6 the back-EMF calculated analytically and that calculated using FEM are compared with the approximated values as calculated in (34) to (36). As can be seen, the approximated back-EMF values compare extremely well with both the analytical and FEM values.

## V. Torque Calculation

### A. Average Torque

For motor operation with the phase voltage and current in phase or for generator operation with the phase voltage and current 180° out of phase, the average mechanical developed torque can be written as

$$T_{mech} = \frac{3\hat{E}_a\hat{I}_a}{2\omega_{mech}}\ , \tag{41}$$

with $\hat{E}_a$ and $\hat{I}_a$ the peak values of the back-EMF and phase current respectively. Substituting (37), the approximated amplitude value of the back-EMF, into (41), the average torque can be approximated by

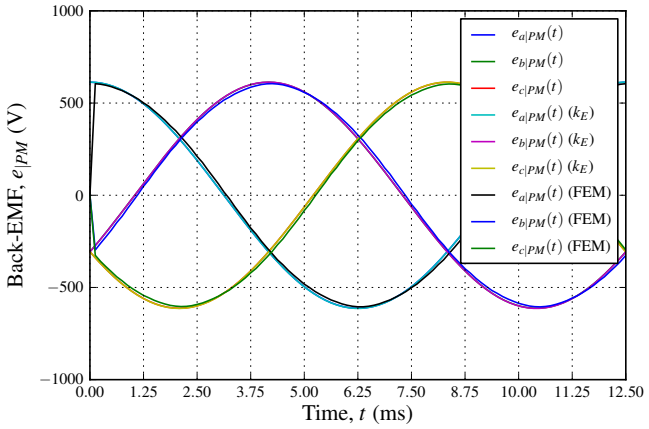


Fig. 6. The back-EMF voltage waveforms.

$$T_{mech} = \tfrac{3}{2}k_E\hat{I}_a \tag{42}$$

$$T_{mech} = k_T\hat{I}_s \tag{43}$$

with the torque constants defined as

$$k_T = k_E = \frac{2qr_n\ell N}{a} k_{w,2}\hat{B}_{r,1} \tag{44}$$

from (40) and the stator current space vector

$$\hat{I}_s = \tfrac{3}{2}\hat{I}_a\ . \tag{45}$$

### B. Torque Ripple

From (23) and assuming balanced sinusoidal current, the three phase current density distribution function can be represented by the following Fourier series,

$$J_z = \begin{cases} -\frac{3q\hat{I}_a N}{ar_n h\pi}\sum_{n=1}^{\infty} k_{w,n}\sin\big(nq\phi + \omega t\big) & \text{for } n = 3k-1 \\ -\frac{3q\hat{I}_a N}{ar_n h\pi}\sum_{n=2}^{\infty} k_{w,n}\sin\big(nq\phi - \omega t\big) & \text{for } n = 3k-2 \end{cases}\ . \tag{46}$$

with $k \in \mathbb{N}_1$ for both cases and $k_{w,n}$ the winding factor for all '$n$' space harmonics.

The Lorentz method for the calculation of the mechanical torque, in integral form, can be given by the following equation

$$T_{mech} = \ell\int_{r_n-\frac{h}{2}}^{r_n+\frac{h}{2}}\int_0^{2\pi} r^2 J_z B_r\, d\phi\, dr\ , \tag{47}$$

with $\ell$ the active stator length.

Solving this equation, again with $n{=}2m$, yields the following solution

$$T_{mech} = -\frac{3q\ell N\hat{I}_a}{ar_n h}\sum_{m=1,5,7,\ldots}^{\infty} k_{w,2m}R_m S_m \tag{48}$$

with $k \in \mathbb{N}_1$ and

$$R_m = \int_{r_n-\frac{h}{2}}^{r_n+\frac{h}{2}} r^2 \cdot \frac{mp(C_m^{III} r^{mp} + D_m^{III} r^{-mp})}{r}\, dr \tag{49}$$

$$= mp\left[\frac{C_m^{III} r^{mp+2}}{mp+2} - \frac{D_m^{III} r^{-mp+2}}{mp-2}\right]_{r_n-\frac{h}{2}}^{r_n+\frac{h}{2}} \tag{50}$$

and

$$S_m = \begin{cases} \cos\big((m-1)p\omega_{mech}t\big) & \text{for } m{=}6k{+}1,\ k \in \mathbb{N}_0 \\ \sin\big((m+1)p\omega_{mech}t\big) & \text{for } m{=}6k{-}1,\ k \in \mathbb{N}_1 \end{cases} \tag{51}$$

and is displayed in Fig. 7 together with the torque calculated using FEM, as well as the average torque calculated by (43).

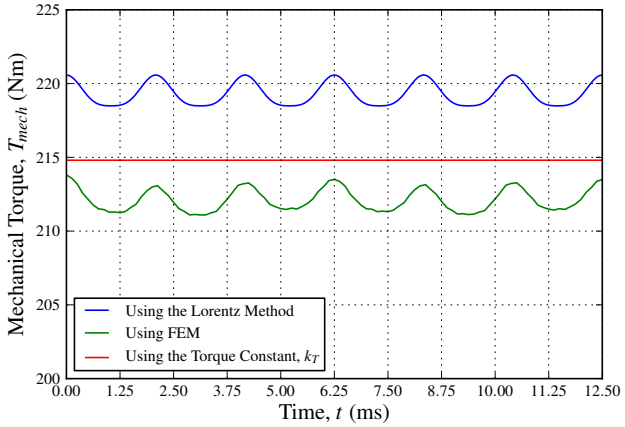


Fig. 7. The calculated torque waveforms.

The Lorentz method for the calculation of the torque compares well with that done using FEM, and is only 3.3% higher due to the 3% higher flux density of the analytically calculated radial flux density. This is quite acceptable considering the fact that saturation in the rotor yokes is ignored. It was however decided to test our theory that the difference in the torque calculation between the analytical and the FEM method is due to yoke saturation, by increasing the yoke thickness, $h_y$, to 20 mm.

As expected the analytical solution was exactly the same, but the FEM solution was surprisingly only 0.5 % higher. The remaining 3.5 % difference can thus not be attributed to yoke saturation. After considering various options, it was decided to also change the coercivity of the PMs used from 1,050,000 A/m to 1,114,084 A/m that would basically result in a relative recoil permeability for the PMs, $\mu_{r_{recoil}} = 1.0$.

Again, the analytical solution was exactly the same, due to the fact that it only makes use of the remanent flux density value of the PMs and always assumes a relative recoil permeability of unity, see Tabel I. The FEM solution, as shown in Fig. 8, is now almost identical to the analytical solution, except for a low frequency oscillation.

In spite of the low frequency oscillation in the FEM solution to the ripple torque, the magnitude of the ripple torque component of the analytical solution is calculated at 1.0% and compares extremely well with the FEM value of 1.1 %. However from (51) it is clear that only sixth order harmonics should be present in the ripple torque output. A harmonic analysis of both the analytical and FEM

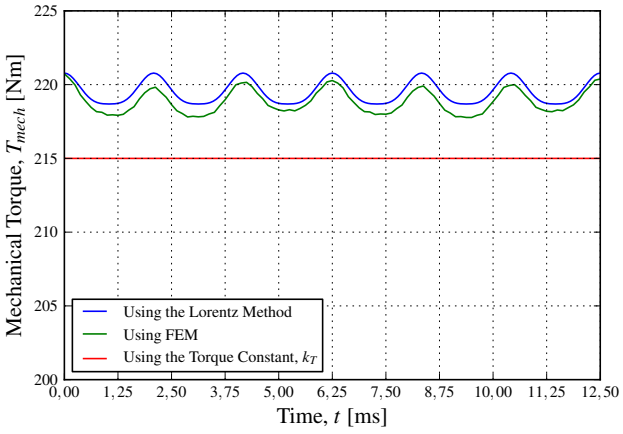


Fig. 8. The calculated torque waveforms with a yoke thickness, $h_y$ = 20 mm and a recoil permeability for the PMs, $\mu_{r_{recoil}} = 1.0$.

result are shown in Fig. 9. From the harmonic analysis it can be seen that the sixth and twelfth harmonics are indeed dominant, with the rest of the harmonics, except for the second harmonic in the FEM solution, being relatively small FEM "noise" components. However another FEM solution done in SEMFEM, a propriety FEM package used by Stellenbosch University, see [16], did not yield a second harmonic component.

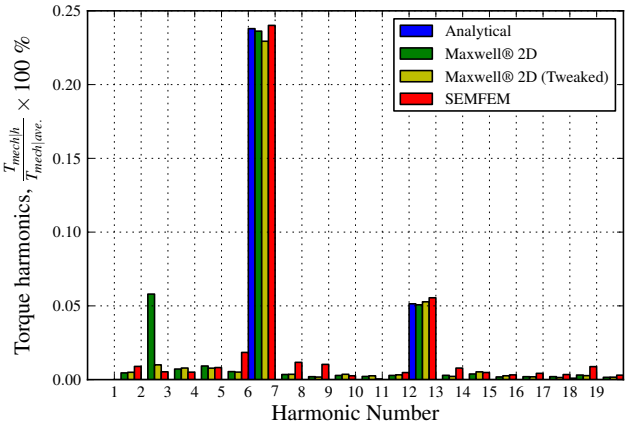


Fig. 9. The harmonic spectrum of the ripple torque.

After consultation with the technical support of the commercial FEM package used, they advise us to "tweak" the FEM model so that the coils are, "not touching the master and slave boundaries" [sic]. This solution, also shown in Fig. 9 eliminated the second order harmonic component so that only the sixth order harmonics remained as was shown by (51). Furthermore, with only the sixth and twelfth harmonic dominant, it implies that the $C_m^{III}$ and $D_m^{III}$ coefficients only need to be solved up to $m$=13 to accurately predict the amplitude and shape of the torque ripple component.

## VI. Conclusions

In this paper it was shown how the radial flux density in the stator region of a RFAPM machine can be calculated analytically, using the subdomain analysis method. With the analytical solution being more than two orders of magnitude faster than the FEM solution, the analytical solution provides us with a quick and easy way in which to determine the

optimum pole arc width of the PMs used that would result in a quasi sinusoidal radial flux density distribution in the centre of the stator region.

Even with non-overlapping winding, a sinusoidal radial flux density distribution results in a very simple solution to the back-EMF solution of the RFAPM machine, from which a voltage constant, similar that that used in traditional brushless DC machines, can be derived. The voltage constant is also equal to the torque constant, so that the torque of the machine can be expressed in terms of the stator current space vector.

It was also shown that for the analytical solution to be accurate, the recoil permeability of the PMs should ideally be unity. However for the N48 NdFeB magnets used, the analytical solution resulted in 3.0 % error when compared the the FEM solution. Saturation of the rotor yokes only accounted for a 0.5 % error in the analytical torque calculation.

Finally it was shown that only sixth order harmonics will be present in the ripple torque component, with the sixth and the twelfth harmonic components being dominant. It must be noted that this will only be true provided that the stator currents are perfectly balanced and sinusoidal.

## REFERENCES


[1] P. J. Randewijk, M. J. Kamper, and R. J. Wang, "Analysis and Performance Evaluation of Radial Flux Air-Cored Permanent Magnet Machines with Concentrated Coils," in *Power Electronics and Drive Systems, 2007. PEDS '07. 7th International Conference on*, 2007, pp. 189–195.

[2] M. J. Kamper, R.-J. Wang, and F. G. Rossouw, "Analysis and Performance of Axial Flux Permanent-Magnet Machine With Air-Cored Non-overlapping Concentrated Stator Windings," *Industry Applications, IEEE Transactions on*, vol. 44, no. 5, pp. 1495–1504, 2008.

[3] J. Cros and P. Viarouge, "Synthesis of high performance PM motors with concentrated windings," *Energy conversion, ieee transactions on*, vol. 17, no. 2, pp. 248–253, 2002.

[4] T. F. Chan and L. L. Lai, "An Axial-Flux Permanent-Magnet Synchronous Generator for a Direct-Coupled Wind-Turbine System," *Energy Conversion, IEEE Transactions on*, vol. 22, no. 1, pp. 86–94, 2007.

[5] J. A. Stegmann and M. J. Kamper, "Design Aspects of Double-Sided Rotor Radial Flux Air-Cored Permanent-Magnet Wind Generator," *IEEE Transactions on Industry Applications*, vol. 47, no. 2, pp. 767–778, Mar. 2011.

[6] R.-J. Wang, M. J. Kamper, K. der Westhuizen, and J. F. Gieras, "Optimal design of a coreless stator axial flux permanent-magnet generator," *Magnetics, IEEE Transactions on*, vol. 41, no. 1, pp. 55–64, 2005.

[7] Z. Q. Zhu, L. J. Wu, and Z. P. Xia, "An Accurate Subdomain Model for Magnetic Field Computation in Slotted Surface-Mounted Permanent-Magnet Machines," *Magnetics, IEEE Transactions on*, vol. 46, no. 4, pp. 1100–1115, 2010.

[8] E. Starschich, A. Muetze, and K. Hameyer, "An Alternative Approach to Analytic Force Computation in Permanent-Magnet Machines," *Magnetics, IEEE Transactions on*, vol. 46, no. 4, pp. 986–995, 2010.

[9] P. Virtic, P. Pisek, M. Hadziselimovic, T. Marcic, and B. Stumberger, "Torque Analysis of an Axial Flux Permanent Magnet Synchronous Machine by Using Analytical Magnetic Field Calculation," *Magnetics, IEEE Transactions on*, vol. 45, no. 3, pp. 1036–1039, 2009.

[10] C.-C. Hwang, P.-L. Li, F. C. Chuang, C.-T. Liu, and K.-H. Huang, "Optimization for Reduction of Torque Ripple in an Axial Flux Permanent Magnet Machine," *Magnetics, IEEE Transactions on*, vol. 45, no. 3, pp. 1760–1763, 2009.

[11] L. J. Wu, Z. Q. Zhu, D. A. Staton, M. Popescu, and D. Hawkins, "Comparison of Analytical Models of Cogging Torque in Surface-Mounted PM Machines," *IEEE Transactions on Industrial Electronics*, vol. 59, no. 6, pp. 2414–2425, Jun. 2012.

[12] P. Kumar and P. Bauer, "Improved Analytical Model of a Permanent-Magnet Brushless DC Motor," *Magnetics, IEEE Transactions on*, vol. 44, no. 10, pp. 2299–2309, 2008.

[13] S. R. Holm, H. Polinder, and J. A. Ferreira, "Analytical Modeling of a Permanent-Magnet Synchronous Machine in a Flywheel," *Magnetics, IEEE Transactions on*, vol. 43, no. 5, pp. 1955–1967, May 2007.

[14] K. I. Laskaris and A. G. Kladas, "Permanent-Magnet Shape Optimization Effects on Synchronous Motor Performance," *IEEE Transactions on Industrial Electronics*, vol. 58, no. 9, pp. 3776–3783, Sep. 2011.

[15] M.-F. Hsieh and Y.-C. Hsu, "A Generalized Magnetic Circuit Modeling Approach for Design of Surface Permanent-Magnet Machines," *IEEE Transactions on Industrial Electronics*, vol. 59, no. 2, pp. 779–792, Feb. 2012.

[16] S. Gerber, J. M. Strauss, and P. J. Randewijk, "Evaluation of a hybrid finite element analysis package featuring dual air-gap elements," in *Electrical Machines (ICEM), 2010 XIX International Conference on*, 2010, pp. 1–6.



**Peter Jan Randewijk** (M'07) received the B.Eng., M.Eng. and Ph.D. degrees in Electrical Engineering from Stellenbosch University in 1992, 1996 and 2012 respectively. From 1995 till 2002 he worked at various companies, starting with the development of traction systems, designing of missile servo drives in the aerospace and defence industry, manufacturing and commissioning of UPS & PSU systems and finally in the design and commissioning of industrial automation and drive systems in the food and beverage sector. In 2002 he joined Stellenbosch University as senior lecturer in power electronics and electrical drive systems. His research is currently focused on smart, renewable, energy efficient energy conversion.

**Maarten Jan Kamper** (SM'08) received the M.Sc. (Eng) and Ph.D. (Eng) degrees from the Stellenbosch University, South Africa, in 1987 and 1996, respectively. In 1989, he joined the academic staff of the Department of Electrical and Electronic Engineering, Stellenbosch University, where he is currently a Professor of electrical machines and drives. His research area is computer-aided design and the control of reluctance, permanent magnet, and induction electrical machine drives, with applications in electric transportation and renewable energy. Prof. Kamper is a South African National Research Foundation supported scientist and a registered Professional Engineer in South Africa.